Research paper

Overconstrained coaxial design of robotic legs with omni-directional locomotion

Yuping Gu [a,b], Shihao Feng [a], Yuqin Guo [a], Fang Wan [a], Jian S. Dai [a,c], Jia Pan [b], Chaoyang Song [a,d,e,*]

[a] Southern University of Science and Technology, Shenzhen, Guangdong, China
[b] The University of Hong Kong, Hong Kong Special Administrative Region of China
[c] King's College London, London, United Kingdom
[d] Shenzhen Key Laboratory of Biomimetic Robotics and Intelligent Systems, Shenzhen, Guangdong, China
[e] Guangdong Provincial Key Laboratory of Human-Augmentation and Rehabilitation Robotics in Universities, Shenzhen, Guangdong, China

ARTICLE INFO

ABSTRACT

While being extensively researched in literature, overconstrained linkages' engineering potential is yet to be explored. This study investigates the design of overconstrained linkages as robotic legs with coaxial actuation starting with the simplest case, Bennett linkage, to establish the theoretical foundations and engineering advantages of a class of overconstrained robots. We proposed a parametric design of the spatial links and joints in alternative forms so that one can fabricate these overconstrained limbs via 3D printing and then attach the linkage coaxially to a pair of servo actuators as a reconfigurable leg module. We adopted multi-objective optimization to refine the design parameters by analyzing its manipulability metric and force transmission, enabling omni-directional ground locomotion projected from a three-dimensional surface workspace. The proposed prototype quadruped was capable of omni-directional locomotion and had a minimal turning radius (0.2 Body Length) using the fewest actuators. We further explored the kinematics and design potentials to generalize the proposed method for all overconstrained 5R and 6R linkages, paving the path for a future direction in overconstrained robotics.

1. Introduction

Walking upright on two legs distinguished the first hominids from the four-legged apes, making bipedalism the most fundamental human characteristic [1]. When designing robots, researchers aim to balance agile locomotion and payload bearing for legged robots [2] but focus on dexterous manipulation and object handling for armed ones [3]. Although this is not the case for all kinematic variations [4], open-chain mechanisms are a common choice for robotic manipulators due to the anthropomorphic resemblance to human arms [5], aiming at dexterous motion at the end-effector to handle objects while being mounted on a fixed base [6]. However, designs for legged robots often prefer closed-chain mechanisms to provide redundant support and reliable motion to handle their body weight during locomotion [7]. In this way, motors for legged robots can be arranged near the body, instead of on the knee joint, using the extra links and joints in closed-chain mechanisms to achieve lower leg inertia for agile motion [8]. As a result, planar four-bar linkage with parallel joint axes [9–11], and its design variations [12,13], become a preferred choice of mechanism due to its simplicity and reliability at a low cost in manufacturing, computation, and control for common legged robots [14].

---

* Corresponding author at: Southern University of Science and Technology, Shenzhen, Guangdong, China.
  E-mail address: songcy@ieee.org (C. Song).

A quick inspection of the four-bar linkage kinematics with only revolute joints reveals solutions other than the typical case with parallel joint axes, including the Bennett linkage with skewed twist angles [15] and the spherical case with intersection joint axes [16]. The spherical four-bar linkages have been widely adopted in medical robots, where the intersected joint axes provide a convenient workspace at a remote, virtual center that can be placed coincidentally to the target area inside the human body for surgical operations [17]. However, there remains a research gap in a wide engineering application of the Bennett linkages, or the overconstrained linkages in general, even though it is one of the simplest revolute-only spatial linkages with the least number of links.

The Bennett linkage needs to satisfy the geometrical conditions in the Bennett Ratio, which is a proportional relationship between the link length against the sine of twist angle. It belongs to a class of spatial mechanisms with specifically designed geometry, making these linkages movable with full-cycle motion but classified as overconstrained under Kutzbach–Grubler's mobility criterion. Besides the Sarrus linkage [18,19] and the Double-Hooke's joint [20], there remains a limited adoption of overconstrained linkages in the engineering design of modern machinery [21–23]. Early efforts have been made on the discovery of the specific geometric conditions that formulate various designs of overconstrained $5R$ and $6R$ linkages [24,25], and till now [26–28]. The more critical research value of overconstrained linkages lies in their underlying mathematics supporting the fundamental research in the kinematic representation of rigid-body motion, advancing the scientific understanding and engineering design of modern machinery and robotics [29]. For example, overconstrained linkages have been used extensively as the target mechanism for analysis during the development of screw theory [30,31] and dual quaternions [32] for machinery [33] and robotics [34].

In this study, we aim at filling the research gap in the engineering design of overconstrained linkages by investigating its research and applied potentials in the design of legged robots. We proposed an alternative form of the Bennett linkage with coaxial actuation as a novel design for robotic legs with omni-directional ground locomotion projected from a three-dimensional surface workspace. In the rest of this study, Section 2 briefly reviews the four-bar linkages in legged robots, presents the overconstrained coaxial leg design using Bennett linkage, and analyzes the robotic interpretation of the kinematics. Section 3 presents the multi-objective design optimization of the leg design based on manipulability metrics and force transmission. Experiment results and discussion are enclosed in Section 4. Section 5 presents the conclusion, limitation, and future work, which concludes this study.

2. Overconstrained coaxial design

2.1. Four-bar linkages in robotic legs

Four-bar linkages are widely adopted in robot design [35–37]. As mentioned earlier, recent advances in the study of leg structure commit to designing the robotic leg with low inertia and placing the actuators in the proximity of the body. Therefore, the four-bar linkages and their variations become a preferred design for power transfer with the motors coaxially located at the hip of each leg. For example, the MIT Cheetah and Cheetah 2 [8,38] are quadruped robots with series configuration legs that adopted the planar four-bar linkage to actuate the knee joint remotely. Furthermore, the ATRAIS is a 3D-capable biped robot with a hip joint and parallel four-bar linkage-based leg [39] which was in a parallel configuration. Although the parallel architectures have a relatively small workspace compared to the serial ones of the same size, lots of efforts have been made to adopt them as robotic legs due to their performance in terms of stiffness, accuracy, and payload [4,40]. Other examples include the Minitaur [14] and the Stanford Doggo [10], which are quadruped robots with symmetric four-bar linkage-based legs, as well as the SpaceBok [9] with the parallelogram based ones.

Kinematically, the parallelogram planar four-bar linkage is equivalent to a particular case of the Bennett linkage defined by the geometric constraints [15] illustrated in Fig. 1. When $\alpha = \beta = 0/\pi$, all joint axes become parallel when the twist angles are set to zero (resulting in a zero-Bennett-Ratio design), making it effectively a parallelogram planar four-bar linkage. Given such an underlying relationship, one follow-up question is whether the Bennett linkage or overconstrained linkages, in general, can be used as a novel leg mechanism for advanced robots.

Hence, the Bennett linkage was chosen in this study as the first example to demonstrate our proposed design strategy for overconstrained robots in this study for its simplicity in design as well as a generalization to the class of Bennett-based linkage family. Also, the Bennett linkage contains only four physical links, making it comparable in engineering design to most robotic legs that are already well-known, including the planar four-bar ones which are mentioned above and spherical four-bar ones. In the meanwhile, the Bennett linkage is also the building block for a class of Bennett-based linkage family, which contains a large number of $5R$ and $6R$ designs in literature [41].

2.2. Coaxial motor arrangement

Recent success in legged robots widely adopted planar four-bar mechanisms and their variations, where the coaxial arrangement of motors become a primary choice in engineering design with reliable and robust performance within a compact form factor [9,10,14]. There are generally two configurations for coaxial motor arrangements. One is *decoupled motor arrangement* with two independent drives both mounted on the robot chassis where the output flanges are arranged opposite to each other, such as Ghost robotics' Minitaur [14] and ETH's SpaceBok [9]. An alternative design is to use belt transmission to relocate the two drives on the same side of the chassis for a compact design [10,42]. Another configuration is *coupled motor arrangement* that achieves coupled actuation with one drive mounted on the flange of another drive fixed on the robot chassis, such as MIT Cheetah3 [13]. This is a popular design with a much-improved form factor but requires coupled actuation.
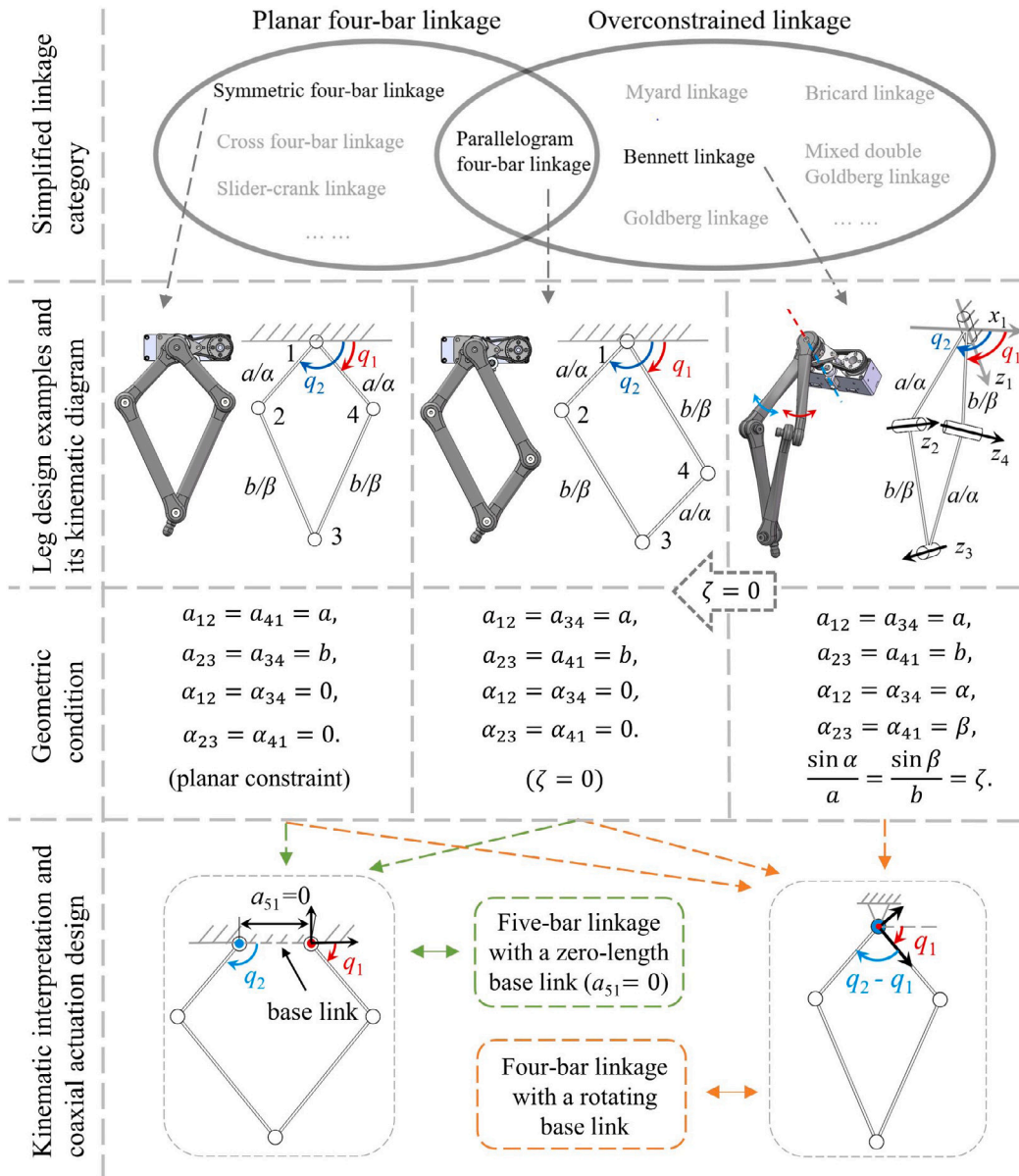
Fig. 1. Review of robotic leg mechanisms with coaxially arranged actuators. And a/α refers to the length and twist angle of the link. When the Bennett-Ratio equals to zero ($\zeta = 0$), the Bennett linkage degenerate into the parallelogram planar four-bar linkage. Note that planar four-bar linkage designs are kinematically equivalent to a planar five-bar linkage with a zero-length base link. The spatial four-bar leg design proposed in this study adopts an alternative interpretation by viewing the coaxial arrangement as a four-bar linkage with a rotating base.

Considering the kinematic resemblance between the overconstrained and planar linkages, we propose to use a similar coaxial motor arrangement for driving overconstrained linkages as the mechanism for robotic limbs. Shown in Fig. 1 is a review of design comparison using the decoupled motor arrangement as an example to demonstrate different linkage attachments. In this case, both links immediately attached to the fixed axis are independent driving links, which can be attached with two separate motors for rotary inputs. For a planar four-bar linkage, such a decoupled coaxial motor arrangement can be kinematically interpreted as a five-bar planar linkage with a zero-length ground link. However, when it comes to the overconstrained linkages, the kinematic interpretation of this configuration should be summarized as a four-bar linkage with a rotating base or with a fixed axis (see Fig. 1). Because when the overconstrained linkages are extended to the $5R$ and $6R$ cases, they are still one-DoF mechanisms, distinct from their planar counterparts.

Another advantage of the above kinematic interpretation is that we can leverage the closure equation of various linkage mechanisms to analyze the corresponding robotic legs' kinematics. Since traditional overconstrained linkage kinematics usually
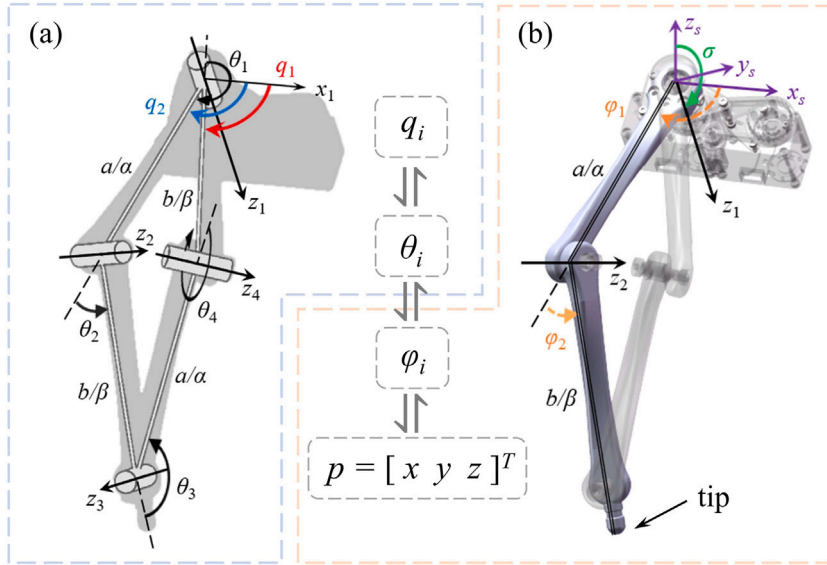
Fig. 2. Kinematic diagram of the Bennett linkage (left) and kinematic diagram of the equivalent open-chain representation (right). q_i, θ_i and φ_i are the actuator joint space, linkage joint space and equivalent open-chain's joint space, respectively, as well as p is the task space (3D coordinate of tip).

consider the relationship between joint angle θ, there remains a gap in formulating the kinematics for robotic applications when these closed-chain mechanisms are involved. For the above reason, taking the fundamental Bennett linkage as an example, a generalization of the kinematic analysis method is proposed in Fig. 2. The coaxial motor arrangement enables two motors as dual inputs for the leg mechanism, namely q_1 and q_2, respectively. We formalize the method shown in Fig. 2 as the technique of *equivalent open-chain*, which views a closed-loop linkage with a remote motor arrangement as an open-chain in serial arrangement with a virtual motor attached to each joint. As a result, the equivalent joint angle φ is defined by the corresponding joint angle θ in linkage analysis obtained from the closure equations. A general expression of equivalent joint angle φ_i can be written as:

$$\varphi_i(q) = f_\varphi(\theta_i) = f_\varphi \left[f_{\theta_i}(\theta_1) \right] = f_\varphi \left\{ f_{\theta_i}[f_{\theta_1}(q)] \right\}, \tag{1}$$

where $f_y(x)$ indicates a mapping relation from x to y and q is the actuator's input angle ($q = [q_1 \; q_2]^T$). Then, using the product of exponential (POE) formula [34], we can write the forward kinematics of the equivalent open-chain's tip as:

$$T(q) = e^{[S_1]\varphi_1} e^{[S_2]\varphi_2} ... e^{[S_n]\varphi_n} P_0, \tag{2}$$

where $S_i \in \mathbb{R}^6$ is the initial velocity screw axis of z_i and $P_0 \in SE(3)$ is the initial position of the defined tip. Both of these are defined in the world coordinate system $\{s\}$. Noted that above formula is suitable for any one-DoF single-loop close-chain linkage mechanism with a rotating base.

2.3. Kinematic analysis of the robotic bennett leg

The resultant pipeline for kinematic analysis is to find the transformation from the motor angles q to the linkage's revolute variables θ, then to the equivalent open-chain's revolute variables in φ. Then through the expressions of φ, we can carry on with the kinematic analysis of the robotic leg using classical robotics modeling methods.

Fig. 2(a) shows the schematics of the Bennett linkage as a leg mechanism and the equivalent open-chain of the robotic Bennett leg is shown in Fig. 2(b). We can look up the closure equations of the Bennett linkage [43] as the following:

$$\theta_1 + \theta_3 = 2\pi, \; \theta_2 + \theta_4 = 2\pi, \tag{3}$$

$$\tan \frac{\theta_1}{2} \tan \frac{\theta_2}{2} = \frac{\sin \frac{1}{2}(\beta + \alpha)}{\sin \frac{1}{2}(\beta - \alpha)} = K, \tag{4}$$

where K is a constant.

Via the above equations and the general sequence of derivation (Eq. (1)), the equivalent joint angle φ_1 and φ_2 in Fig. 2(b) can be expressed in the function of actuators' angle q as the following:

$$\begin{cases} \varphi_1(q) = \theta_1 - (\pi - q_1) = q_2, \\ \varphi_2(q) = \theta_2 = 2 \arctan(-K \tan \frac{q_2 - q_1}{2}). \end{cases} \tag{5}$$

Then, referring to Eq. (2), the forward kinematics of the equivalent open-chain's tip can be obtained as the following:

$$T(q) = e^{[S_1]\varphi_1} e^{[S_2]\varphi_2} P_0,$$ (6)

where

$$S_1 = \begin{bmatrix} 0 \\ -\sin\sigma \\ \cos\sigma \\ 0 \\ 0 \\ 0 \end{bmatrix}, \quad S_2 = \begin{bmatrix} 0 \\ -\sin(\alpha+\sigma) \\ \cos(\alpha+\sigma) \\ 0 \\ -a\cos(\alpha+\sigma) \\ -a\sin(\alpha+\sigma) \end{bmatrix}, \quad P_0 = \begin{bmatrix} 1 & 0 & 0 & a+b \\ 0 & 1 & 0 & 0 \\ 0 & 0 & 1 & 0 \\ 0 & 0 & 0 & 1 \end{bmatrix}.$$ (7)

According to the geometric constraint, the inverse kinematics problem can be resolved as:

$$\begin{cases} q_1 = \arctan\left(\frac{y\cos\sigma + z\sin\sigma}{x}\right) - 2\arctan\left(\frac{K\left(b\sin\beta \pm \sqrt{b^2\sin^2\alpha - (y\sin\sigma - z\cos\sigma)^2}\right)}{-y\sin\sigma + z\cos\sigma}\right) \\ \qquad + \arcsin\left(\frac{(y\sin\sigma - z\sin\sigma)\cot\alpha}{\sqrt{x^2 + (y\cos\sigma + z\sin\sigma)^2}}\right) - \pi, \\ q_2 = \arctan\left(\frac{y\cos\sigma + z\sin\sigma}{x}\right) + \arcsin\left(\frac{(y\sin\sigma - z\sin\sigma)\cot\alpha}{\sqrt{x^2 + (y\cos\sigma + z\sin\sigma)^2}}\right) - \pi. \end{cases}$$ (8)

The symbol '±' indicates that there are multiple solutions of q_1 and the adopted solution can be obtained by the forward kinematics formula. Instead of giving the three-dimensional coordinates of the tip, which is located on the 3D coupled workspace exactly, we derived an explicit mapping relationship of tip's coordinate, enclosed in Appendix A.

The space Jacobian $J_s(\varphi)$ of the equivalent representation relates the equivalent joint rate vector $\dot{\varphi}$ to the tip's velocity screw $\mathcal{V} \in \mathbb{R}^6$. Then, the leg Jacobian $J(q)$, a 6×2 matrix determined by actuators' angle q, can be obtained by multiplying $J_s(\varphi)$ and the derivative of $\varphi(q)$ with respect to q. Therefore, the velocity screw $\mathcal{V}$ of tip can also be presented as the following:

$$\mathcal{V} = J_s(\varphi)\dot{\varphi} = \begin{bmatrix} J_{s1} & J_{s2} \end{bmatrix} \dot{\varphi} = \begin{bmatrix} J_{s1} & J_{s2} \end{bmatrix} \begin{bmatrix} \frac{\partial\varphi_1}{\partial q_1} & \frac{\partial\varphi_1}{\partial q_2} \\ \frac{\partial\varphi_2}{\partial q_1} & \frac{\partial\varphi_2}{\partial q_2} \end{bmatrix} \dot{q} = J(q)\dot{q},$$ (9)

where

$$J_{si} = Ad_{e^{[S_1]\varphi_1}\dots e^{[S_{i-1}]\varphi_{i-1}}}(S_i).$$ (10)

2.4. Robotic Bennett leg and prototype design

The overconstrained geometry usually means an increased precision in the fabrication and assembly of the linkage, limiting the specific overconstrained linkages to be used. This study proposes a general design method of the overconstrained linkages for robotic usage, leveraging 3D printing for rapid prototyping. As shown in Fig. 3, a common overconstrained link consists of the following geometry features: link length, twist angle, and a zero joint offset, which the corresponding alternative form can equivalently replace with a given assembly clearance and loft-connected joint parts. Each revolute joint comprises two up–down staggered joint parts designed for specific usages, such as common joints with an extensive range of motion, connecting to the actuators or forming the leg tip. Therefore, proper joint part (upper or down) arrangement of each linkage is vital to successfully form the single loop mechanism and reduce the possibility of interference between the links. In practice, short links prefer to use the same type of joint parts (upper–upper or down–down) to avoid collision, and links with large twist angles prefer to use the design in diverse ones. Hence, the proposed alternative form links were parameterized and generalized to any twisted link in overconstrained linkages with a concise and straightforward configuration despite the joint parts being specially designed. As shown in Figs. 16 and 18, this method can be widely used in designing various overconstrained linkages (4R, 5R, even the 6R cases) for robotic usage, which were practically verified and tested via 3D-printed prototypes.

In this study, PA-12 (or Nylon 12) is selected as the printing material for its mechanical strength and high tenacity. The FEA (Finite Element Analysis) result in Fig. 3 shows the strain and stress on the overconstrained leg, which is applied a 20 N ground reaction force (the overall weight of the prototype robot) as load. The maximum stress of the 3D-printed leg is 4.45 MPa, which is much smaller than the material's yield strength (48 MPa), showing the reliability of this design for the prototype testing. The analysis result shows that the maximum stresses concentrate on the thigh links, indicating a better mechanical performance and lighter weight with an asymmetrical design of the links.

As shown in Fig. 4, the proposed robotic leg design adopted the Bennett linkage as the leg mechanism with coaxial actuating in a relocated, decoupled arrangement. Link 41, one of the driven links, is directly actuated by the servo I, which is rigidly connected to the servo via an inner shaft. Link 12, another driven link, was actuated quasi-directly by the remote servo II via the 1:1 time belt drive transmission and was connected to a hollow shaft which is bearing supported by the inner shaft and outer housing. A pair of pulleys were added to adjust the pretension force. In this configuration, axis z_1 was defined as the fixed axis to the robot body, resulting in axis z_3 close to the tip. The robotic tip is a small part stretching from link 23, which is covered with a silicone case to increase the coefficient of friction.
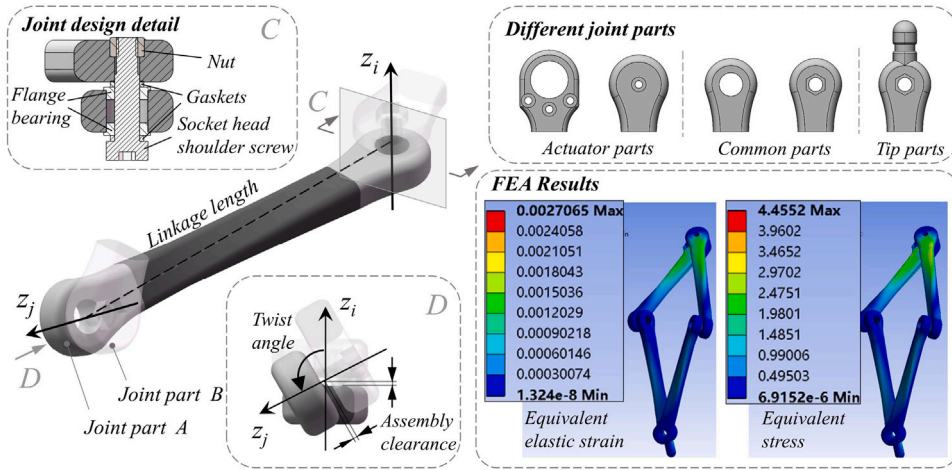
Fig. 3. Twisted link design for rapid prototyping via 3D printing. The finite element analysis result demonstrate the reliability.
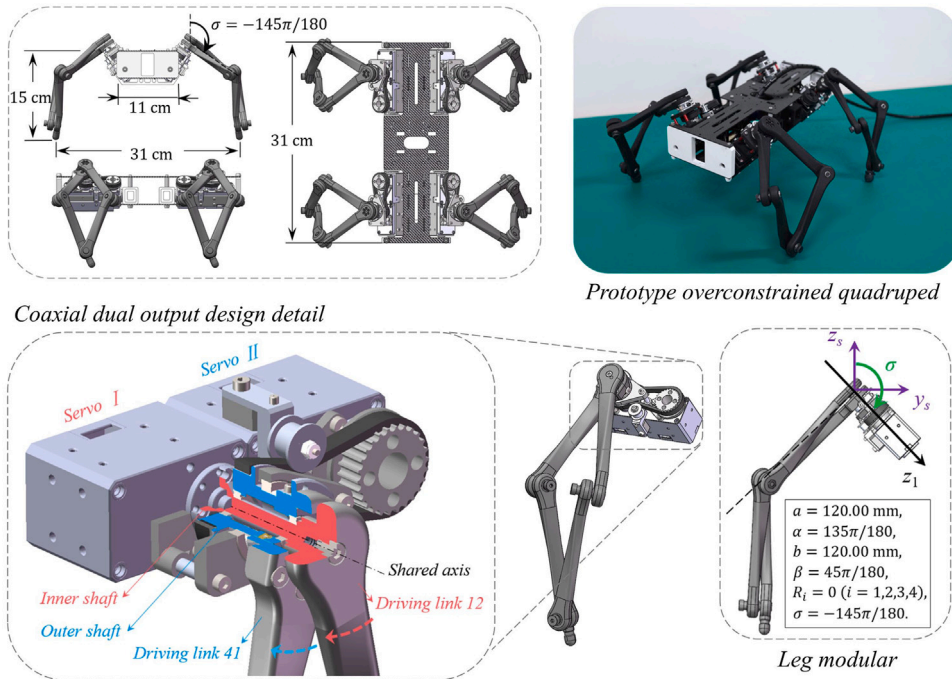

Fig. 4. The design of the robotic Bennett leg with coaxially arranged actuation and the design parameters of proposed omni-directional quadruped prototype. σ is a constant parameter, named hip frame assembly angle.

Then we introduce an essential design parameter, namely the hip frame assembly angle (σ), which is defined as the constant angle between z_s and z_1 in Fig. 4. For the planar two-DoF robotic leg, this parameter is usually set close to $\pi/2$ to obtain the perpendicular workspace. However, when it comes to the overconstrained leg, the fixed assembly angle geometrically represents the tilt extent of the workspace. As illustrated in Fig. 5, by combining the additional rotational degrees of freedom with overconstrained spatial linkage, the resulting workspace was a two-dimensional manifold in the three-dimensional euclidean space as well as maintaining the constant angle with the world coordinate. The shape of the workspace is similar to a half-cut-away torus, indicating that it was generated by rotating a semicircular line in 3D space.

As shown in Fig. 4, we designed and manufactured the prototype quadruped robot, which is assembled by modular overconstrained robotic leg with coaxial dual output configuration. The design detail of the modular can be referred to in Fig. 4. All the modules are fixed at the main body of quadruped with the same hip frame assembly angle (σ). Each leg has two Dynamixel XM-430 W210 servos, and each tip is coated by a hemispherical silicone case fabricated by Ecoflex 00-30. An OpenCM 9.04 broad was
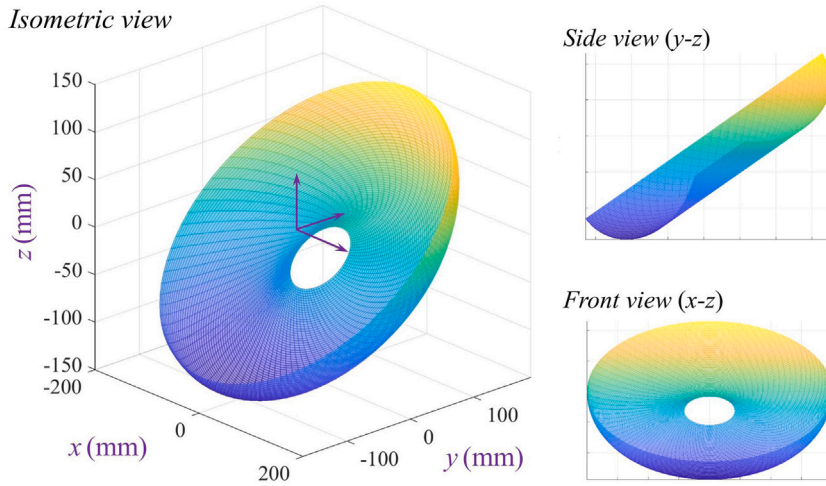
Fig. 5. The theoretical workspace of the proposed robotic Bennett leg.

selected as the micro-controller. The robot has 31 cm body length, 11 cm body width, and 31 cm total width at its rest pose with a weight of 1.6 kg.

3. Multi-objective design optimization

3.1. Manipulability metric

Manipulability of the end-effector can visualize mobility in an arbitrary direction. Yoshikawa proposed the most commonly used definition of manipulability [44], which is represented in a m-dimensional Euclidean space for the end-effector. The discussion of manipulability and performance indices with full rank Jacobian are extensively covered in the literature [45,46], however, which of the coupled 3D motion is relatively limited. The linear velocity vector $\dot{p} = \begin{bmatrix} \dot{x} & \dot{y} & \dot{z} \end{bmatrix}^T$ are more intuitive for robotic applications comparing with the six-dimensional velocity screw $\mathcal{V}$. By converting the leg Jacobian into an analytical form, we obtain that:

$$\dot{p} = J_a(q)\dot{q}, \tag{11}$$

in which the analytical Jacobian $J_a(q) \in \mathbb{R}^{3 \times 2}$. Although J_a is not a square matrix, we can still find the left Moore–Penrose generalized inverse of J_a due to the overconstrained geometric constraint. Then the unit joint rates condition $\|\dot{q}\| = 1$ can be written as:

$$1 = \dot{q}^T \dot{q} = \left(J_a^\dagger \dot{p}\right)^T J_a^\dagger \dot{p} = \dot{p}^T \left(J_a J_a^T\right)^\dagger \dot{p} = \dot{p}^T A^\dagger \dot{p}. \tag{12}$$

If J_a is full rank, the matrix $A = J_a J_a^T \in \mathbb{R}^{3 \times 3}$ is semi-positive definite, with two positive eigenvalues and a zero eigenvalue. Therefore, even the overconstrained robotic legs are not in the singular configuration, and the traditionally defined manipulability $m = \sqrt{\det(A)}$ always equals zero on account of the restricted coupled motion in the three-dimensional space. As illustrated in Fig. 6, defining λ_1 and λ_2 as the positive eigenvalues of A (v_1 and v_2 are the corresponding eigenvectors), the manipulability ellipsoid applies the v_1 and v_2 as the directions of the principal axes, with the principal semi-axes length $\sqrt{\lambda_1}$ and $\sqrt{\lambda_2}$. Furthermore, the manipulability ellipsoid is always located on the tangent plane of the workspace.

The direction of the zero eigenvalue's eigenvector is normal to the tangent plane, which indicates the geometrical motion characteristic of the overconstrained legs. Therefore, the manipulability of overconstrained robotic leg should be defined as:

$$m_o = \sqrt{\lambda_1 \lambda_2}, \tag{13}$$

where λ_i is the positive eigenvalue of matrix A. If the number of positive eigenvalues is less than two, then $m_o = 0$, indicating that the configuration is singular. Note that m_o is proportional to the area of the ellipse, which can be simply defined as one of the manipulability indexes in a single point of the workspace. Since a global dexterity index has been presented in [47], one of the global manipulability indexes can also be defined as:

$$\epsilon_1 = \frac{1}{W} \iint_W m_o \, dW, \tag{14}$$

where W is the workspace area. Another widely used manipulability index is the inverse condition number κ^{-1}, referring to the isotropic motion ability in the corresponding configuration and is defined as:

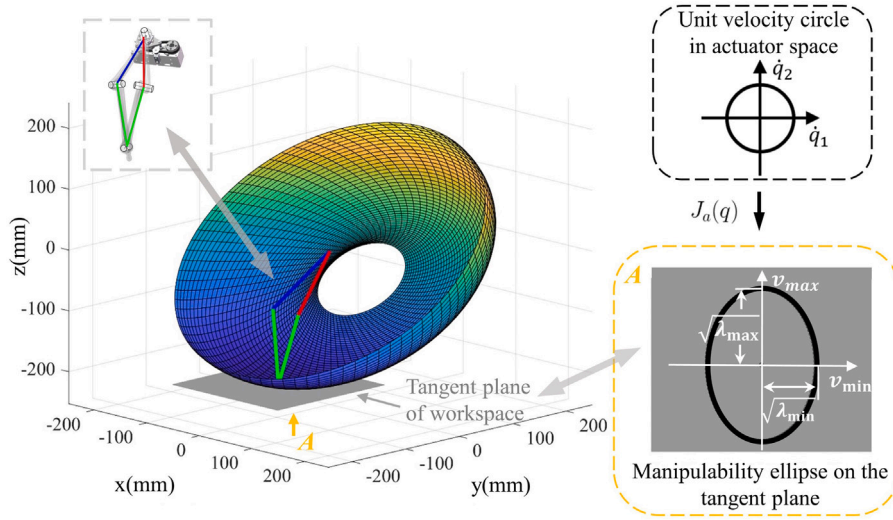$$\kappa^{-1} = \sqrt{\frac{\lambda_{\min}}{\lambda_{\max}}}, \tag{15}$$

Fig. 6. Manipulability ellipsoid of the overconstrained robotic leg at a specific configuration. Note that the manipulability ellipsoid is always on the tangent plane of the workspace.

in which $\lambda_{\min}$ and $\lambda_{\max}$ are the positive eigenvalue values of A when the configuration is not singular. If the robotic leg can instantaneously move equally well in the tangential direction, then $\lambda_{\min} = \lambda_{\max}$ and $\kappa^{-1} = 1$, referring to an isotropic configuration. If there are not enough positive eigenvalues, then $\kappa^{-1} = 0$, revealing a singularity. Then, another global manipulability index can be given by:

$$\epsilon_2 = \frac{1}{W} \iint_W \kappa^{-1} dW. \tag{16}$$

3.2. Force transmission

The Force transmission metric measures the ability of ground reaction force generation. We can effectively decrease the motor torque requirement by optimizing this metric. This study defines the force transmission metric as the mean motor torque to generate a vertical ground reaction force of 20 N in the workspace. The ground reaction force can be estimated by using the Jacobian,

$$\tau = J_a^T(q)f, \tag{17}$$

where the ground reaction force $f = [0, 0, -20]^T$.

Thus, the global force transmission metric can be formulated as

$$\epsilon_3 = \frac{1}{W} \iint_W |\tau_i(q)| dW. \tag{18}$$

If $a = b$, the two motors equally contribute to the tip and the workspace is plane symmetry, resulting in the same metric value whatever τ_i is chosen as τ_1 or τ_2.

3.3. Design optimization

The overconstrained linkages are advanced in generating fascinating spatial motions while suffering from complex geometric conditions that are not intuitive for engineering design and integration in modern machinery and robotics. In this study, to address this challenge, we proposed a novel optimization strategy for overconstrained robotic legs by combining a simplified form of the manipulability metric ϵ_1 that describes its workspace characteristics, an isotropic metric ϵ_2 that describes the legs forward and lateral motion characteristics, and a force transmission metric ϵ_3 to account for its dynamic performance while interacting with the ground. Among the three metrics, ϵ_1 is adapted from a classical definition of the manipulability metric in literature [44]. ϵ_2 is used for the overconstrained robotic leg to demonstrate its omni-directional locomotion capability even though it is actuated by only two motors, reflecting its advantage over other planar leg mechanisms which usually require an additional motor. Furthermore, ϵ_3 is used here to guarantee a general working performance of the leg's dynamics, capable of generating the necessary ground reaction force.

The final objective function can be defined as the combination of normalized metrics. The min–max normalization method [48] was used to normalize the metrics for having equivalent contributions to the objective. And the optimization problem can be formulated as

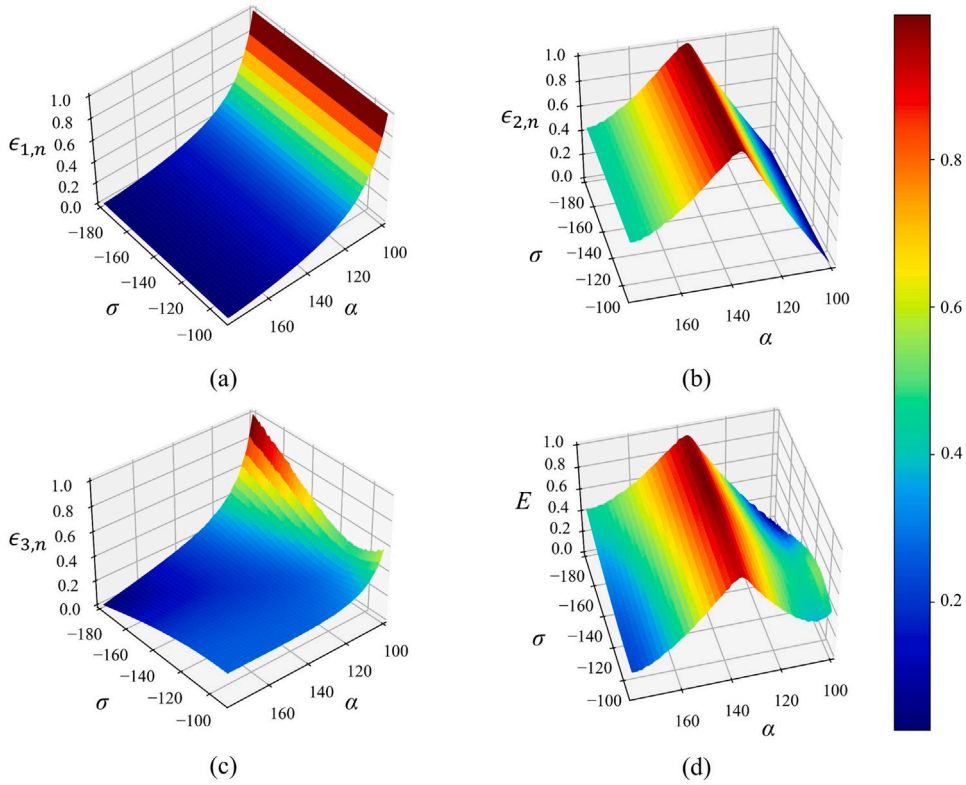$$\max \quad E = w_1 \epsilon_{1,n} + w_2 \epsilon_{2,n} - w_3 \epsilon_{3,n} \tag{19}$$

Fig. 7. Normalized performance metrics in the parameter space. (a) Manipulability metric. (b) Isotropic metric. (c) Force transmission metric. (d) Total objective function value.

$$\text{s.t.} \quad \begin{cases} \alpha + \beta = 2\pi \\ 2\pi/9 \leq \alpha < \pi \\ -\pi \leq \sigma \leq -\pi/2 \\ 0 \leq q_2 - q_1 \leq \pi \end{cases} \tag{20}$$

where w_1, w_2, and w_3 are the weights and $\epsilon_{i,n}$ $(i = 1, 2, 3)$ is the corresponding normalized metric, which is in range of 0 to 1. In our design, the weights are typically set as 1, 1, and 1, respectively. The maximum leg length is set as 0.24 m $(b = 0.24 - a)$, and a reasonable range for alpha and sigma is set. For the geometric symmetry of the Bennett linkage, the length of four links is set to be equal $(a = b)$. In this case, the workspace area becomes the largest [42]. The equality constraints are given by Eq. (20). Therefore, the optimization variables reduce from $[a, \alpha, \sigma]$ to $[\alpha, \sigma]$, in which α is the twist angle of linkage and σ is the hip frame assembly angle.

The manipulability and the inverse condition number are the metrics that describe the mechanism's characteristics, and it is not related to the orientation (σ) w.r.t hip frame assembly angle. Both α and σ contribute to the force transmission metrics. The step of parameters range is set to one degree, resulting in a small parameter set that can be solved using an exhaustive method [49]. The calculation of the three performance metrics is estimated by the mean of the sampling points in the workspace. The uniform sampling in joint space always leads to an uneven distribution in cartesian space, so we conduct a uniform sampling in cartesian space [50]. The number of sampling points is set to 10,000. The results of the three performance metrics are normalized and shown in Fig. 7(a), (b) and (c), respectively. Fig. 7(d) shows the result of the total cost. The density distribution map of the total cost is illustrated in Fig. 8, and the optimal solution is $[\alpha = 135°, \sigma = -147°]$. For practical fabrication, a nearby parameter set $[\alpha = 135°, \sigma = -145°]$ is selected and it is marked as a triangle in Fig. 8. Fig. 9 presents the corresponding metrics under the optimum parameter within the workspace. According to the total objective function value, an optimal area of workspace is obtained, which is shown in Fig. 9(d). Therefore, we define a much-reduced region as the engineering workspace for trajectory planning which is illustrated in Fig. 10.

4. Experiment results and discussion

4.1. Omni-directional locomotion with robotic Bennett legs

To demonstrate the omni-directional locomotion capability of the overconstrained quadruped robot with limited actuating DoFs of each leg, we proposed three different trajectories for corresponding tasks, including forwarding motion (moving along the x-axis),
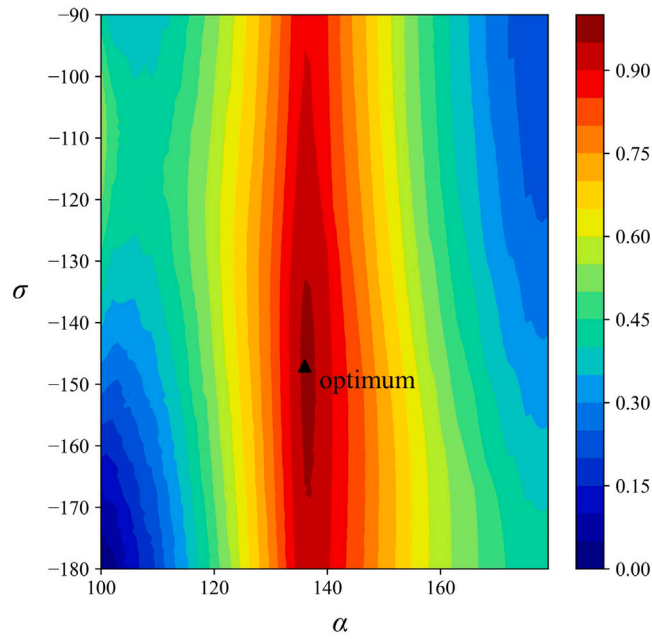
Fig. 8. Multi-objective optimization result ($[\alpha = 135°, \sigma = -145°]$) in a 2D map.
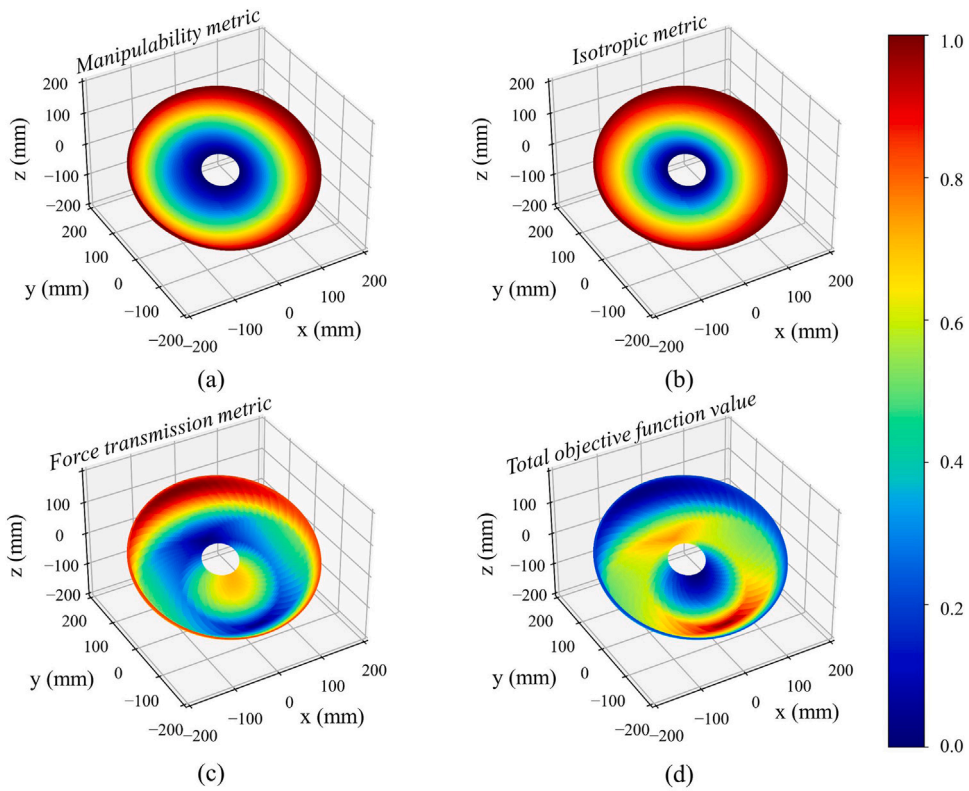

Fig. 9. Normalized performance metrics in the theoretical workspace. (a) Manipulability metric. (b) Isotropic metric. (c) Force transmission metric. (d) Total objective function value.

lateral motion (moving along the y-axis), and pivot steering (revolving around the z-axis), respectively. As shown in Fig. 10, the stance phase of the trajectories was planned along the locomotion direction straightly, while the swing phase is a spatial curve
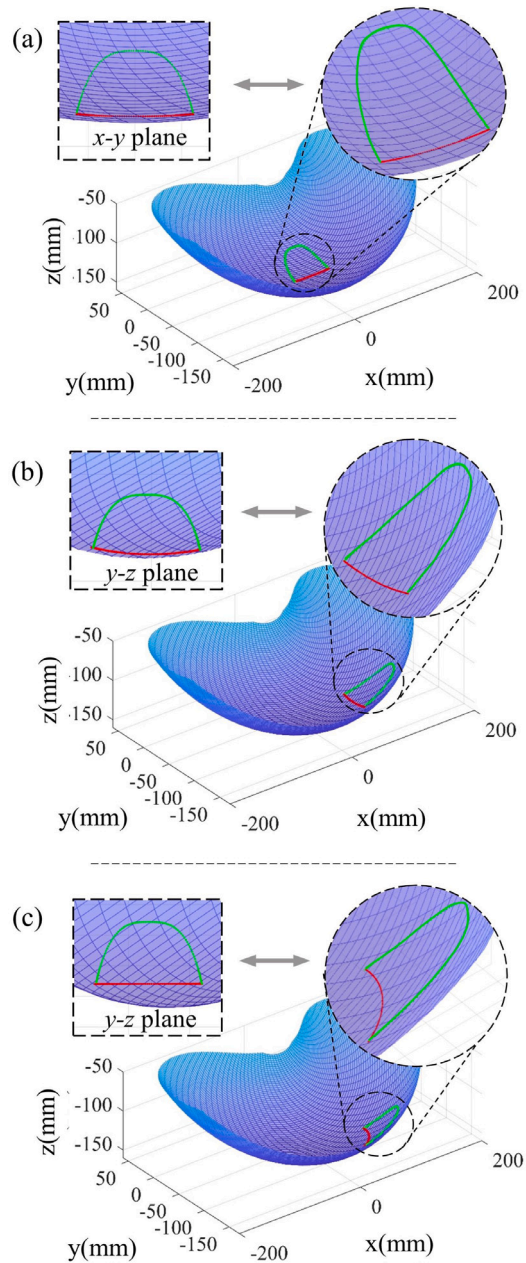
Fig. 10. Three different trajectories used in the experiment within the engineering workspace. (a) Forward locomotion trajectory. (b) Lateral locomotion trajectory. (c) Pivot steering trajectory.

whose projection in the locomotion plane is a segmented sinusoid. Note that the overconstrained robot leg will bend inwards or straighten outward with an elevating tip as a coupled motion in 3D space during the swing phase. Therefore, selecting the steep part of the workspace to generate the trajectory would effectively avoid the tip being applied extra side force caused by unexpected contact with the ground during the swing phase due to the particular coupled spatial motion. Additionally, the trajectory planning method based on compound cycloid [51] is adopted to improve the smoothness and reduce mechanical shock.

As illustrated in Fig. 11(a), the overconstrained quadruped robot was capable of common forward trotting like its counterparts with planar linkages. Furthermore, due to the application of overconstrained linkage, our robot is also competent for the tasks such as lateral trotting in Fig. 11(b) and pivot steering in Fig. 11(c), indicating the omni-directional locomotion property. Compared with existing 8-DoF quadruped robots, for example, the Stanford Doggo [10] and the Ghost Robotics' Minitaur [14], which may get in trouble with steering and lateral locomotion, our design could achieve the omni-directional locomotion without introducing
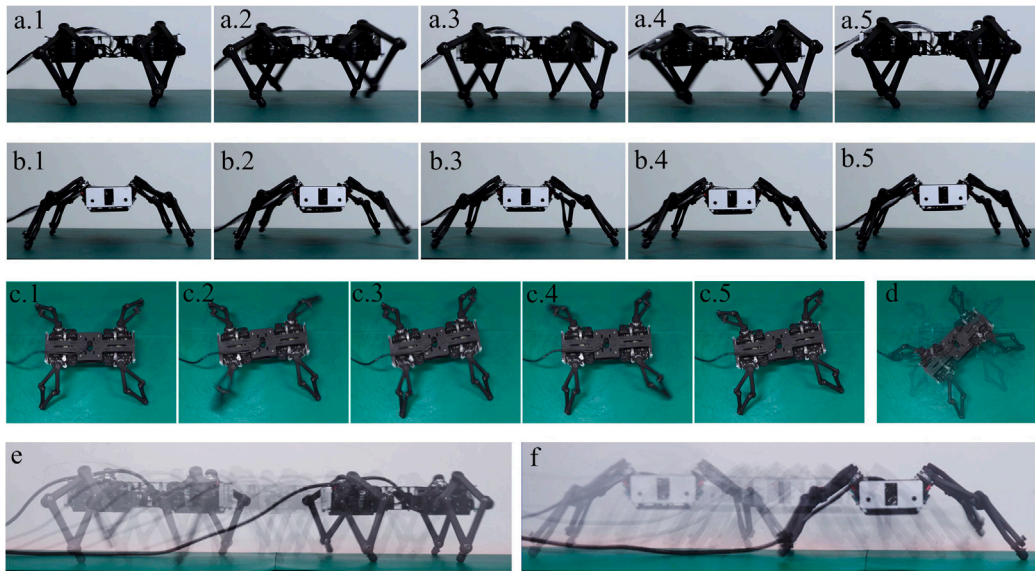
Fig. 11. Image sequence of different locomotion demo, indicating the omni-directional mobile capability. (a) Forward motion. (b) Lateral motion. (c) Pivot steering. (d–f) Overlaid snapshots of corresponding locomotion.

additional actuation. A significant qualitative performance improvement was achieved by importing the twist angle to the planar four-bar linkage design, especially by adopting the spatial overconstrained design.

An inertial measurement unit (IMU) was assembled to measure the body's roll and pitch angle, which can be leveraged to evaluate the quasi-static locomotion during the experiments. As Fig. 12(a) and (b) shown, the fluctuation ranges of roll angle and pitch angle were about 4° and 6°, respectively, for both forward trotting and lateral trotting. Moreover, when it came to pivot steering, the fluctuation ranges of roll and pitch angles were still not significant, which is about 13° (roll angle) and 10° (pitch angle), as shown in Fig. 12(c). The phase period was set as 0.7 s for all the gaits. The locomotion speed of forward-moving was 0.1 m/s, similar to the lateral-moving speed, indicating equivalent mobility in different directions. On the other hand, the angular velocity of pivot steering was 30°/s, which can be obtained from Fig. 12(d). Furthermore, the periodic ups and downs of the rotation angle (yaw angle) were caused by the approximately circular stance phase, which can be resolved by improving the trajectory planning method. In short, this experiment indicated that the overconstrained quadruped robot was capable of relatively steady omni-directional locomotion.

Another experiment was also carried out to demonstrate the omni-directional locomotion of our design, especially the turning capability. Fig. 13 shows the experiment setup for measuring the turning radius of the proposed overconstrained quadruped. We use Intel RealSense Camera D435i to track the pose of the quadruped via the ArUco marker [52] on its back. The camera was configured to capture frames at a resolution of 1280×720 under a framerate of 30 FPS. Fig. 14 presents the position of the robot's CoM when it turns from 0° to 360°, anti-clockwise. Although we demonstrated that our design was capable of pivot steering, small displacements would still exist during turning due to the slippage between feet and ground and the system error. Thus, the turning radius was computed as the circle radius which could include all tracked CoMs. As shown in Fig. 14, the minimum turning radius of our design was estimated as 0.2 Body Length (BL) within a 30 mm circle marked in red.

For comparison, several quadruped robots were listed in Fig. 15. Notably, turning radius values were only given for quadruped robots with two active DoFs per leg, even though all of them have additional DoFs on their back or trunk. The Cheeta-Cub-S [53] is a small quadruped with an active spine-like structure to improve the turning performance. Although it is configured with additional spine DoF and has a relatively high locomotion speed, its turning radius is still measured at 2.48 BL. SQuRO [54] and NeRmo [55] are bio-inspired small size quadruped robots with 12 and 13 DoFs, respectively. With the increased system complexity, these robots have multiple motion modes and smaller turning radii than the Cheeta-Cub-S. However, our proposed quadruped achieved the smallest turning radius (0.2 BL) with the fewest total DoFs for locomotion (8 DoFs) at a relatively high angular velocity (30 deg/s), as shown in Fig. 15. Please note that our design achieves such performance without using any advanced gait pattern or control yet, demonstrating the superior performance of the overconstrained robotic leg in its vanilla form. It appears that after further optimization in control, our robot holds the potential to outperform these state-of-the-art robots in turning speed as well, all thanks to the use of overconstrained linkages as robotic limbs.

4.2. Generalization to overconstrained robotic legs

Similarly, through the derivation in Section 3, one can introduce almost any of the single DoF overconstrained linkages with closed-loop for legged robots, as long as a coaxial arrangement of the actuators is maintained. By modifying the link's geometric
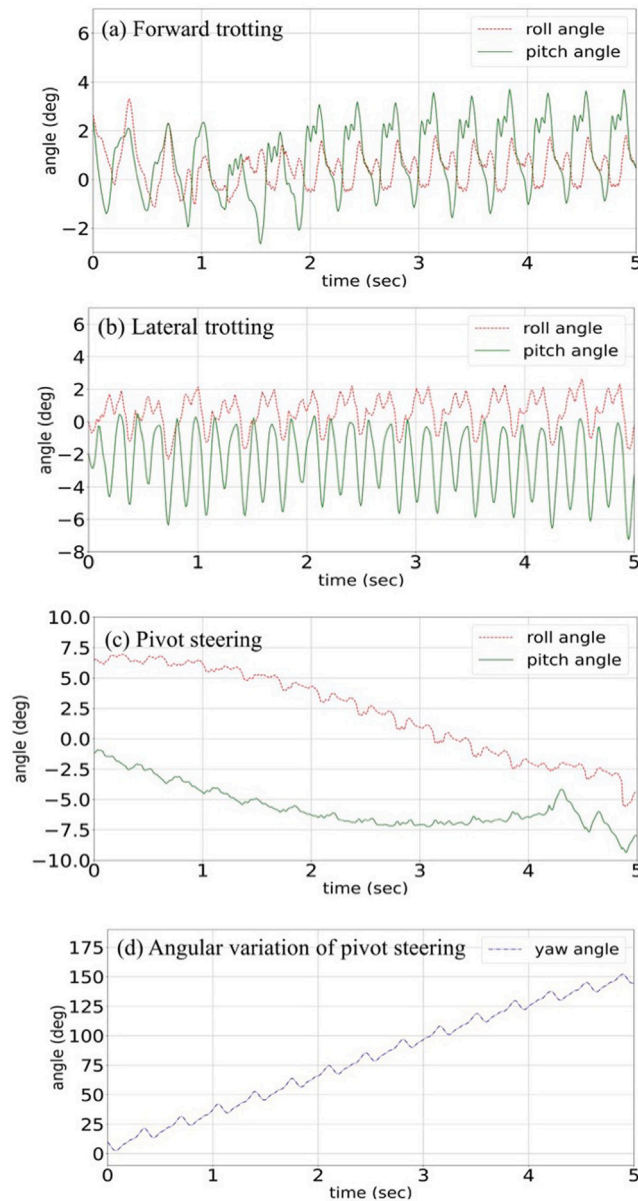
Fig. 12. Measured IMU data of the experiments. (a)–(c) Roll and pitch angle of body during the experiment for different gait. (d) The rotation angle during pivot steering.

constraints, a large pool of design variations exists as closed-loop overconstrained linkages with a single-degree-of-freedom [41,56–58]. For example, one linkage from the family of Goldberg's linkage (5R) and mixed double Goldberg's linkage (6R) was chosen to adapt as the robotic legs with coupled 3D motion. As shown in Figs. 16 and 18, the proposed overconstrained legs leverage our design method and the linkage complexity, which leads to some different performance in terms of stiffness, force transmission, and workspace compared with the robotic Bennett leg. The corresponding derivation is presented in the Appendix B and the workspace is shown in Figs. 20 and 21, respectively. Different overconstrained linkages will form the workspace in various shapes, which are still in the form of coupled space surface and satisfy the above discussion of manipulability and optimization. Additionally, Figs. 17 and 19 illustrate the capability of versatile motions of these two promoted overconstrained robotic legs, which are similar to their Bennett-based former.

However, the increased number of the revolute joint usually means a reduced stiffness of the end effector because of the assembly accuracy and cumulative error. In the presented cases, the overconstrained leg with six revolute joints (6R) may not be so suitable as the robotic leg due to a high amplification factor between the input angle error and output displacement in some specific configuration, which could potentially be resolved by the configuration optimization method to a certain level. In other words,
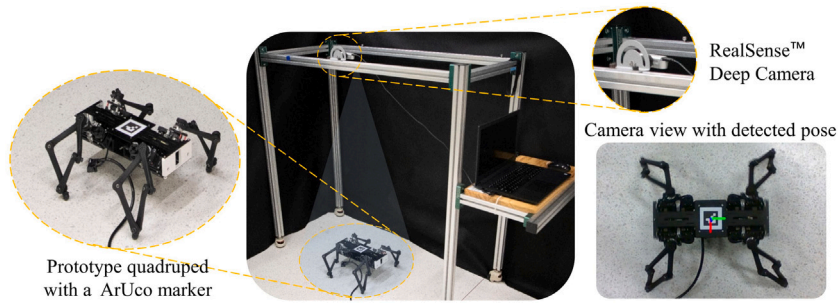
Fig. 13. The experiment setup for measuring the turning radius of our design. An Intel RealSense D435i camera was used to detect the robot's body pose our design during turning. The pose was estimated via the ArUco marker on the center of robot and the marker coordinate system is placed at the center of marker with colored axis directions (X: red, Y: green, Z: blue). (For interpretation of the references to color in this figure legend, the reader is referred to the web version of this article.)
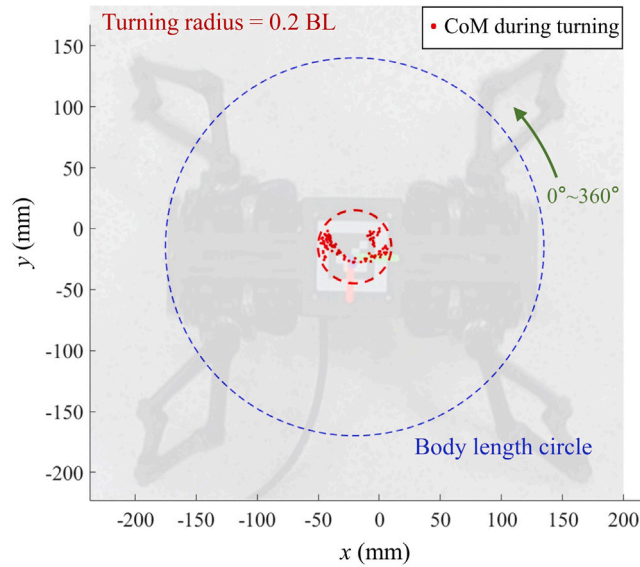

Fig. 14. Experiment results of the proposed quadruped's center of mass (CoM) trajectory during turning, achieving a minimum radius of 0.2 body length (BL) in red dashed circle. (For interpretation of the references to color in this figure legend, the reader is referred to the web version of this article.)
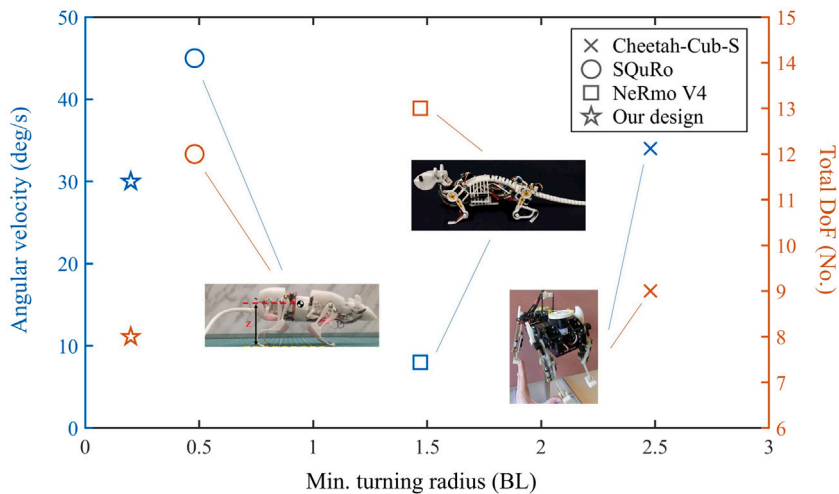

Fig. 15. Comparison of the turning radius of various quadruped robots relative to the angular velocity (left vertical axis) and total DoFs (right vertical axis).
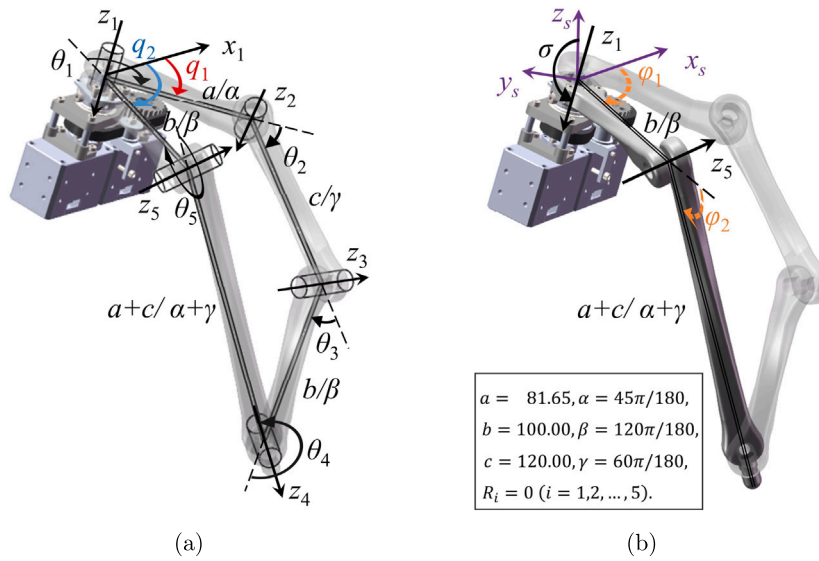
Fig. 16. Proposed 5R overconstrained robotic leg with coaxial configuration. (a) The kinematic diagram. (b) The equivalent open-chain representation.
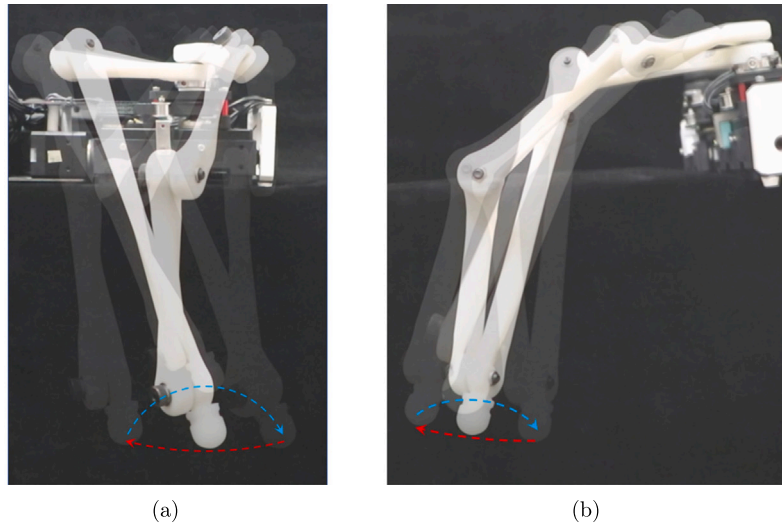

Fig. 17. Trajectories of proposed 5R overconstrained robotic leg. (a) Forward locomotion trajectory (blue: swing phase; red stance phase). (b) Lateral locomotion trajectory. (For interpretation of the references to color in this figure legend, the reader is referred to the web version of this article.)

finding the one among the overconstrained linkages that provides the most balanced benefits for legged robots is a potential research question to be addressed in future work.

Despite the above engineering problem of joint tolerance, the manufacturing challenges of prototyping a particular twist angle, link length, or offset is not an easy task. In this study, we addressed this issue with a few design considerations. Firstly, we leverage the scale effect to reduce the problem with tolerance requirements. The overall robot is designed to be relatively small and lightweight, but the bearings are chosen to be relatively larger in diameter to enhance the linkage's motion. Then, the flexibility is intentionally introduced to the leg by using 3D printed Nylon instead of rigidly fabricated legs made from a metallic material. It provides the necessary structural tolerance without affecting the leg motion. Finally, the joint assembly is carefully tightened to rotate smoothly without too much visible deflection of the links on the joint. As illustrated in Fig. 11, the resultant robot built performs nicely with omni-directional locomotion, which alleviated our concern on this matter.

4.3. Towards overconstrained robotics for advanced engineering

Despite being a vibrant family of mechanism designs with unique constraints in geometry and coupled motions in 3D, the overconstrained linkages are still mainly used for kinematic research with limited robotic systems realization. The overconstrained
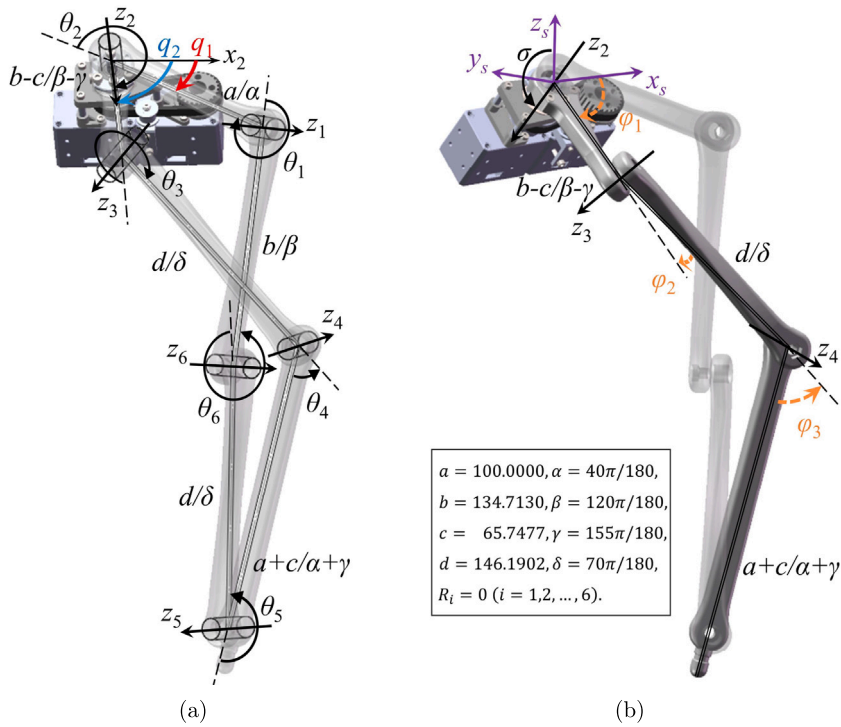
$a = 100.0000, \alpha = 40\pi/180,$
$b = 134.7130, \beta = 120\pi/180,$
$c = 65.7477, \gamma = 155\pi/180,$
$d = 146.1902, \delta = 70\pi/180,$
$R_i = 0 \; (i = 1,2,\dots,6).$

Fig. 18. Proposed 6R overconstrained robotic leg with coaxial configuration. (a) The kinematic diagram. (b) The equivalent open-chain representation.
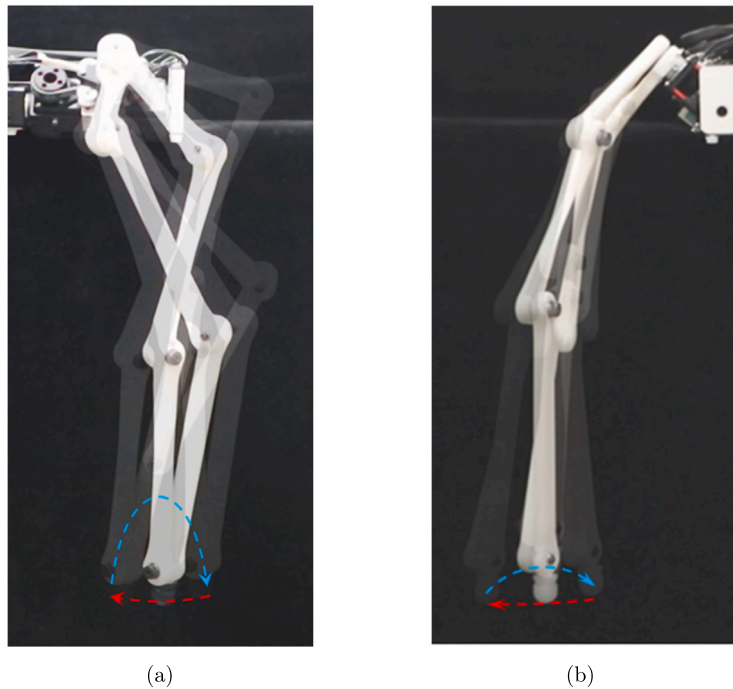

Fig. 19. Trajectories of proposed 6R overconstrained robotic leg. (a) Forward locomotion trajectory (blue: swing phase; red stance phase). (b) Lateral locomotion trajectory. (For interpretation of the references to color in this figure legend, the reader is referred to the web version of this article.)

condition of a linkage is usually defined using the classical Chebychev—Grübler—Kutzbach criterion when the calculated mobility is less than the linkage's actual degree-of-freedoms, which is caused by the particular set of geometric conditions that define the
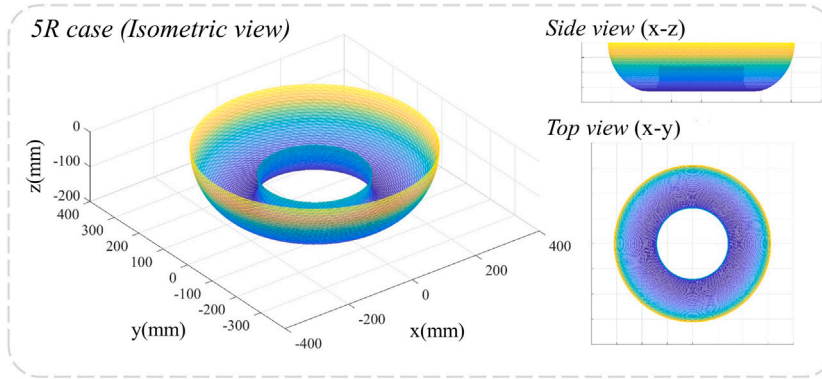
Fig. 20. The theoretical workspace of proposed 5R overconstrained robotic leg.
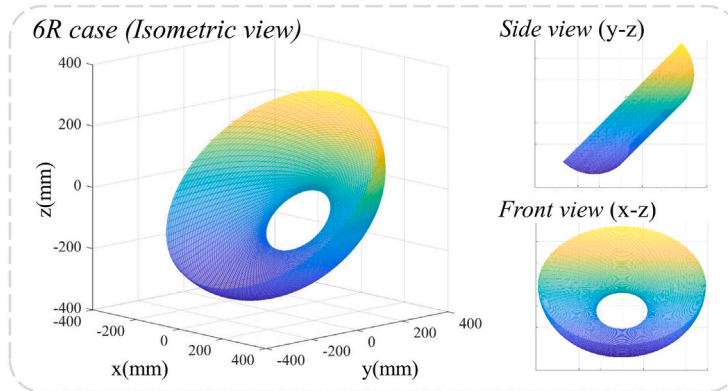

Fig. 21. The theoretical workspace of proposed 6R overconstrained robotic leg.

linkage's kinematic design. In classical research, we usually further narrow down the overconstrained linkages to those that formulate a single loop in topology, jointed by simple revolute pairs only, and movable with only one degree of freedom, including the Bennett-based linkages, Bricard linkages, etc.

In this study, we claim our method to be a generalized solution due to the adoption of a co-axially arranged actuation that is generally applicable to drive any revolute pair. In this way, one actuator drives one link of the revolute pair with another actuator driving the other link of the same revolute pair, resulting in a movable base link. This is counter-intuitive in classical mechanism design, as we usually need to define a fixed base link to describe the relative motion in common linkages. For example, a pair of coaxial drives attached to a planar four-bar linkage (such as Ghost Robotics' Minitaur, or Stanford's Doggo) is kinematically equivalent to a planar five-bar linkage with two DOFs by viewing the base link with a zero-length.

However, as we proposed in this study, we can also attach the coaxial drives to an overconstrained linkage (single-loop linkages with revolute joints only, movable with only one degree of freedom) by driving its base link to be movable as well. In this way, as we have demonstrated in this study, it becomes convenient and practical in engineering to make overconstrained linkages useful for robotic applications without violating the basic scientific principles of linkage kinematics. As we have presented in this study, the resultant design shows superior performance in the legged robot example, making it an interesting and generalized method for developing overconstrained robotics as a potentially new field of research. One can generalize the same principle to all overconstrained linkages to make them engineering useful in robot design.

This study demonstrates a design strategy by leveraging the coaxial motor arrangement for overconstrained linkages as robotic legs. The kinematic formulation in Sections 2.2 and 2.3 demonstrates a practical methodology that translates the structural formulation from closed-loop linkage to open-chain robots, making it convenient to leverage the existing findings in overconstrained kinematics. Combined with the results shown in Sections 4.1 and 4.2, we argue the potential for a research field in overconstrained robotics by using overconstrained linkages to formulate novel robot structures, which are capable of versatile motions in three-dimensional space using fewer actuators.

While the potential advantage of robots with overconstrained linkages is probably a systematic reduction in actuation, the coupled spatial motion generated from these linkages means that it will require careful design and planning of the linkage geometry before making the optimized use of these designs. For example, the coupled motion shown in Fig. 10 exhibited a coupled elevation while the leg is moving back-and-forth or sideways, which needs to be addressed through engineering designs.

On the other hand, one might extend the proposed method in this study for other robot designs, such as novel manipulators and reconfigurable mobile robots [59,60] where agile spatial motions and lightweight design are critical considerations in advanced engineering applications. For example, Huang and Li [61] has proposed using a pair of 6R overconstrained linkage as the wings of a bird. Recently, Yao et al. [19] have proposed a particular integration using Schatz linkage with a compact form factor for backpacking while mobile as a legged robot in multiple terrains. Additionally, there is a class of metamorphic quadruped with moveable trunk [62–64] and introducing the overconstrained linkage into these designs may potentially reduce the number of actuators in trunks. Also, the kinematic bifurcation of the overconstrained linkages could be another topic worth exploring with overconstrained robots, where the overall robot can be reconfigured from one mode to another [56,65].

5. Conclusion and future work

This study explores the coaxial design of the overconstrained linkages for legged robots, achieving omni-directional locomotion via much-reduced actuation, making it a novel mechanism for advanced robots. We developed the generalized methodology for kinematic analysis, design, and optimization of Bennett-based robotic leg, which can also extend to 5R and 6R overconstrained robotic leg cases. We verified the proposed overconstrained robotic leg's omni-directional performance through a quadruped robot prototype. The prototype outperformed the state-of-the-art turning in quadruped robots with a minimum turning radius of 0.2 body length using fewer actuators.

The advanced kinematic behavior derived from its geometrical conditions is a limitation of using overconstrained linkages for novel robotic applications. Modern computational tools are well-equipped to overcome such difficulties once an effective engineering design is determined. Also, the overconstrained geometry usually means increased complexity in control and algorithm design and dynamic modeling. However, modern approaches such as robot learning or Graph-Neural-Networks (GNN) for learning the dynamics [66] instead of analytically derive them for our proposed design. Furthermore, Tan et al. [67] presented a system to automatically design agile locomotion for quadruped robots via deep reinforcement learning techniques.

Our future work will develop a modern approach to delving into the dynamics and optimized controller of the quadruped with overconstrained linkages as robotic limbs. We are also interested in developing generative design algorithms to aid the design process with artificial intelligence for overconstrained robots.

Declaration of competing interest

The authors declare that they have no known competing financial interests or personal relationships that could have appeared to influence the work reported in this paper.

Acknowledgment

Appendix A. Explicit mapping relationship of tip's coordinate

As mentioned in Section 2.3, it is not intuitive for us to give a complete tip coordinate, which is located on the 3D coupled workspace precisely, for calculating the inverse kinematics with Eq. (8). Therefore, the trajectory is usually constrained on one projection plane (xy, yz, or xz). Then, the explicit mapping relationship of the tip's coordinate is derived in the following part, with which we can obtain the coupled 3D coordinate of the tip by the given points on the projection plane.

The implicit equation of workspace in Cartesian space is

$$x^2 + (y\sin\sigma - z\cos\sigma)^2 - (\frac{y\cos\sigma + z\sin\sigma}{\tan\beta})^2 - [a + \frac{\sqrt{(b\sin\beta)^2 - (y\cos\sigma + z\sin\sigma)^2}}{\sin\beta}]^2 = 0. \tag{A.1}$$

The corresponding point in workspace can be found out via the implicit equation, then used to solve the inverse kinematics. When planning in yz-plane, we can calculate the x-position through the formula below

$$x = \pm\sqrt{-(y\sin\sigma - z\cos\sigma)^2 + (\frac{y\cos\sigma + z\sin\sigma}{\tan\beta})^2 + [a + \frac{\sqrt{(b\sin\beta)^2 - (y\cos\sigma + z\sin\sigma)^2}}{\sin\beta}]^2}. \tag{A.2}$$

While planning in xy-plane and xz-plane are needed to solve a quartic equation

$$\begin{cases} A_1 z^4 + B_1 z^3 + C_1 z^2 + D_1 z + E_1 = 0, \\ A_2 y^4 + B_2 y^3 + C_2 y^2 + D_2 y + E_2 = 0, \end{cases} \tag{A.3}$$

where

$$\begin{cases} a_0 = \sin^2\sigma - (\frac{\cos\sigma}{\tan\beta})^2 + (\frac{\cos\sigma}{\sin\beta})^2, \\ b_0 = \cos^2\sigma - (\frac{\sin\sigma}{\tan\beta})^2 + (\frac{\sin\sigma}{\sin\beta})^2, \\ c_0 = -\sin 2\sigma(1 + \cot^2\beta) + \frac{1}{\sin^2\beta}, \\ d_0 = -a^2 - b^2 + x^2, \end{cases} \tag{A.4}$$

$$\begin{cases} A_1 = b_0^2, \\ B_1 = 2b_0 c_0 y, \\ C_1 = (2a_0 b_0 + c_0^2)y^2 + 2b_0 d_0 + (\frac{2a\sin\sigma}{\sin\beta})^2, \\ D_1 = 2a_0 c_0 y^3 + (2c_0 d_0 + \frac{4a^2\sin 2\sigma}{\sin\beta})^2 y, \\ E_1 = a_0^2 y^4 + [2a_0 d_0 + (\frac{2a\cos\sigma}{\sin\beta})^2]y^2 + d_0^2 - 4a^2 b^2, \end{cases} \tag{A.5}$$

$$\begin{cases} A_2 = a_0^2, \\ B_2 = 2a_0 c_0 z, \\ C_2 = (2a_0 b_0 + c_0^2)z^2 + 2a_0 d_0 + (\frac{2a\cos\sigma}{\sin\beta})^2, \\ D_2 = 2b_0 c_0 z^3 + (2c_0 d_0 + \frac{4a^2\sin 2\sigma}{\sin\beta})^2 z, \\ E_2 = b_0^2 z^4 + [2b_0 d_0 + (\frac{2a\sin\sigma}{\sin\beta})^2]z^2 + d_0^2 - 4a^2 b^2. \end{cases} \tag{A.6}$$

The real roots of the quartic equation are what we need.

Appendix B. Forward kinematics for proposed 5R and 6R cases

The forward kinematics of illustrated 5R and 6R overconstrained robotic legs (see Figs. 16 and 18) were derived in this section. Like the Bennett-based robotic leg, the focal point is to obtain the equivalent open-chain's joint angle φ in terms of the motor angle q from the adopted linkage's closure equation. All the links we used here share the same Bennett ratio and have zero joint offsets:

$$\frac{\sin\alpha}{a} = \frac{\sin\beta}{b} = \frac{\sin\gamma}{c} = \frac{\sin\delta}{d} \quad \text{and} \quad R_i = 0 \;\; (i = 1, 2, \ldots, 6). \tag{B.1}$$

Firstly, the closure equations of the adopted 5R Goldberg linkage [43] are:

$$\begin{cases} \tan\frac{\theta_1}{2}\tan\frac{\theta_5}{2} = \frac{\sin((\alpha+\beta)/2)}{\sin((\alpha-\beta)/2)} = K_G, \\ \tan\frac{\theta_4}{2}\cot\frac{\theta_1}{2} = \frac{\sin((\alpha+\beta)/2)}{\sin((\alpha-\beta)/2)}, \\ \theta_1 + \theta_3 = \pi \quad \text{and} \quad \theta_2 + \theta_4 + \theta_5 = \pi. \end{cases} \tag{B.2}$$

Then, we can obtain that:

$$\begin{cases} \varphi_1(q) = (\pi - \theta_1) + q_1 = q_2, \\ \varphi_2(q) = 2\pi - \theta_5 = 2\pi - 2\arctan\left(K_G \tan\left((q_2 - q_1)/2\right)\right). \end{cases} \tag{B.3}$$

And the forward kinematics is similar to the form in Eq. (6).

On the other hand, the type II mixed double-Goldberg 6R linkage [41] is selected as the 6R robotic leg case with following closure equations:

$$\begin{cases} \tan\frac{\theta_2}{2} = \frac{K_1}{\tan(\theta_1/2)}, \quad \tan\frac{\theta_3}{2} = \frac{P\cdot\tan(\theta_1/2) - K_2}{\tan(\theta_1/2) + P\cdot K_2}, \\ \tan\frac{\theta_4}{2} = -K_3/P, \quad \tan\frac{\theta_5}{2} = -P\cdot K_4, \\ \tan\frac{\theta_6}{2} = \frac{\tan^2(\theta_1/2) + K_1\cdot K_2 - P\cdot(K_1 - K_2)\tan(\theta_1/2)}{(K_1 - K_2)\tan(\theta_1/2) + P\cdot(K_1\cdot K_2 + \tan^2(\theta_1/2))}, \end{cases} \tag{B.4}$$

Then, the 6R robotic leg's equivalent joint angle φ can be derived as follows:

$$\begin{cases} \varphi_1(q) = q_2, \\ \varphi_2(q) = 2\arctan\left(\frac{-P\cdot K_1 \tan((q_2-q_1)/2) - K_2}{-K_1 \tan((q_2-q_1)/2) + P\cdot K_2}\right) - 2\pi, \\ \varphi_3(q) = 2\arctan\left(-K_3/P\right), \end{cases} \tag{B.5}$$

with

$$\begin{cases} K_1 = \frac{\sin((\beta+\alpha)/2)}{\sin((\beta-\alpha)/2)}, \quad K_2 = \frac{\sin((\gamma+\alpha)/2)}{\sin((\gamma-\alpha)/2)}, \quad K_3 = \frac{\sin((\delta+\alpha)/2)}{\sin((\delta-\alpha)/2)}, \quad K_4 = \frac{\sin((\delta+\gamma)/2)}{\sin((\delta-\gamma)/2)}, \\ P = \frac{(1 - K_3 K_4) \pm \sqrt{(K_3 K_4 - 1)^2 - 4K_1^2 K_3 K_4 \tan^2((q_2-q_1)/2)}}{2K_1 K_2 \tan((q_2-q_1)/2)}. \end{cases} \tag{B.6}$$

Since we have obtained the above formula, the forward kinematics can also be written in the exponential product.

References

[1] N.M. Tanner, et al., On Becoming Human, CUP Archive, 1981.
[2] S. Rezazadeh, A. Abate, R.L. Hatton, J.W. Hurst, Robot leg design: A constructive framework, IEEE Access 6 (2018) 54369–54387.
[3] R.R. Ma, A.M. Dollar, On dexterity and dexterous manipulation, in: 2011 15th International Conference on Advanced Robotics (ICAR), IEEE, 2011, pp. 1–7.
[4] Z. Pandilov, V. Dukovski, Comparison of the characteristics between serial and parallel robots, Fascicule 1 (2014) 2067–3809.
[5] L. Sciavicco, B. Siciliano, Modelling and Control of Robot Manipulators, Springer Science & Business Media, 2001.
[6] C.M. Gosselin, The optimum design of robotic manipulators using dexterity indices, Robot. Auton. Syst. 9 (4) (1992) 213–226.
[7] J. Park, K.-S. Kim, S. Kim, Design of a cat-inspired robotic leg for fast running, Adv. Robot. 28 (23) (2014) 1587–1598.
[8] S. Seok, A. Wang, M.Y. Chuah, D.J. Hyun, J. Lee, D.M. Otten, J.H. Lang, S. Kim, Design principles for energy-efficient legged locomotion and implementation on the MIT cheetah robot, IEEE/ASME Trans. Mechatronics 20 (3) (2014) 1117–1129.
[9] P. Arm, et al., Spacebok: A dynamic legged robot for space exploration, in: International Conference on Robotics and Automation (ICRA), 2019, pp. 6288–6294.
[10] N. Kau, A. Schultz, N. Ferrante, P. Slade, Stanford doggo: an open-source, quasi-direct-drive quadruped, in: International Conference on Robotics and Automation (ICRA), 2019, pp. 6309–6315.
[11] W. Bosworth, S. Kim, N. Hogan, The MIT super mini cheetah: A small, low-cost quadrupedal robot for dynamic locomotion, in: 2015 IEEE International Symposium on Safety, Security, and Rescue Robotics (SSRR), 2015, pp. 1–8.
[12] B. Katz, J. Di Carlo, S. Kim, Mini cheetah: A platform for pushing the limits of dynamic quadruped control, in: 2019 International Conference on Robotics and Automation (ICRA), IEEE, 2019, pp. 6295–6301.
[13] G. Bledt, M.J. Powell, B. Katz, J. Di Carlo, P.M. Wensing, S. Kim, MIT Cheetah 3: Design and control of a robust, dynamic quadruped robot, in: 2018 IEEE/RSJ International Conference on Intelligent Robots and Systems (IROS), IEEE, 2018, pp. 2245–2252.
[14] G. Kenneally, A. De, D.E. Koditschek, Design principles for a family of direct-drive legged robots, IEEE Robot. Autom. Lett. 1 (2) (2016) 900–907.
[15] G.T. Bennett, A new mechanism, Engineering(London) 76 (1903) 777–778.
[16] C. Chiang, On the classification of spherical four-bar linkages, Mech. Mach. Theory 19 (3) (1984) 283–287.
[17] C. Wu, X.-J. Liu, L. Wang, J. Wang, Optimal design of spherical 5R parallel manipulators considering the motion/force transmissibility, J. Mech. Des. 132 (3) (2010).
[18] J. Santiago-Prowald, H. Baier, Advances in deployable structures and surfaces for large apertures in space, CEAS Space J. 5 (2013) 89–115.
[19] S. Yao, R. Liu, Y.-a. Yao, Design and analysis of a multi-mode mobile robot based on Schatz linkages, Mech. Mach. Theory 169 (2022) 104651.
[20] H.-C. Seherr-Thoss, F. Schmelz, E. Aucktor, Universal Joints and Driveshafts: Analysis, Design, Applications, Springer Science & Business Media, 2006.
[21] S. Pellegrino, Deployable Structures, Vol. 412, Springer, 2014.
[22] H. Huang, Z. Deng, B. Li, Mobile assemblies of large deployable mechanisms, J. Space Eng. 5 (1) (2012) 1–14.
[23] Z. You, Motion structures extend their reach, Mater. Today 10 (12) (2007) 52–57.
[24] F.E. Myard, Contribution à la géométrie des systèmes articulés, Soc. Math. France 59 (1931) 183–210.
[25] M. Goldberg, New five-bar and six-bar linkages in three dimensions, Trans. ASME 65 (1943) 649–661.
[26] Y. Chen, Z. You, An extended Myard linkage and its derived 6R linkage, J. Mech. Des. 130 (5) (2008) 052301.
[27] G. Wei, J.S. Dai, Origami-inspired integrated planar-spherical overconstrained mechanisms, J. Mech. Des. 136 (5) (2014) 051003.
[28] G. Wei, J.S. Dai, A spatial eight-bar linkage and its association with the deployable platonic mechanisms, J. Mech. Robot. 6 (2) (2014) 021010.
[29] J. Phillips, Freedom in Machinery: Introducing Screw Theory, Vol. 1, Cambridge University Press, 1984.
[30] K. Waldron, A family of overconstrained linkages, J. Mech. 2 (2) (1967) 201–211.
[31] J.S. Dai, Z. Huang, H. Lipkin, Mobility of overconstrained parallel mechanisms, J. Mech. Des. 128 (1) (2004) 220–229.
[32] A.T. Yang, Application of Quaternion Algebra and Dual Numbers to the Analysis of Spatial Mechanisms (Ph.D. thesis), Columbia University, US, 1963.
[33] K.J. Waldron, G.L. Kinzel, S.K. Agrawal, Kinematics, Dynamics, and Design of Machinery, John Wiley & Sons, 2016.
[34] K.M. Lynch, F.C. Park, Modern Robotics, Cambridge University Press, 2017.
[35] A. Hamon, Y. Aoustin, Cross four-bar linkage for the knees of a planar bipedal robot, in: 2010 10th IEEE-RAS International Conference on Humanoid Robots, IEEE, 2010, pp. 379–384.
[36] J.-S. Zhao, Z.-F. Yan, L. Ye, Design of planar four-bar linkage with n specified positions for a flapping wing robot, Mech. Mach. Theory 82 (2014) 33–55.
[37] F.Y. Chen, Gripping mechanisms for industrial robots: an overview, Mech. Mach. Theory 17 (5) (1982) 299–311.
[38] S. Seok, A. Wang, D. Otten, S. Kim, Actuator design for high force proprioceptive control in fast legged locomotion, in: 2012 IEEE/RSJ International Conference on Intelligent Robots and Systems, IEEE, 2012, pp. 1970–1975.
[39] J.A. Grimes, J.W. Hurst, The design of ATRIAS 1.0 a unique monopod, hopping robot, in: Adaptive Mobile Robotics, World Scientific, 2012.
[40] J.-P. Merlet, Parallel Robots, Vol. 128, Springer Science & Business Media, 2005.
[41] C. Song, Y. Chen, A family of mixed double-Goldberg 6R linkages, Proc. R. Soc. A 468 (2139) (2012) 871–890.
[42] S. Feng, Y. Gu, W. Guo, Y. Guo, F. Wan, J. Pan, C. Song, An overconstrained robotic leg with coaxial quasi-direct drives for omni-directional ground mobility, in: 2021 IEEE International Conference on Robotics and Automation (ICRA), IEEE, 2021, pp. 11477–11484.
[43] J.E. Baker, The Bennett, Goldberg and Myard linkages—in perspective, Mech. Mach. Theory 14 (4) (1979) 239–253.
[44] T. Yoshikawa, Manipulability of robotic mechanisms, Int. J. Robot. Res. 4 (2) (1985) 3–9.
[45] J.P. Merlet, Jacobian, manipulability, condition number, and accuracy of parallel robots, J. Mech. Des. 128 (1) (2005) 199–206.
[46] J. Lee, A study on the manipulability measures for robot manipulators, in: Proceedings of the 1997 IEEE/RSJ International Conference on Intelligent Robot and Systems. Innovative Robotics for Real-World Applications. IROS'97, Vol. 3, IEEE, 1997, pp. 1458–1465.
[47] C. Gosselin, J. Angeles, A global performance index for the kinematic optimization of robotic manipulators, 1991.
[48] R.T. Marler, J.S. Arora, Function-transformation methods for multi-objective optimization, Eng. Optim. 37 (6) (2005) 551–570.
[49] M. Russo, et al., Kinematic analysis and multi-objective optimization of a 3-UPR parallel mechanism for a robotic leg, Mech. Mach. Theory 120 (2018) 192–202.
[50] P. Diaconis, S. Holmes, M. Shahshahani, Sampling from a manifold, in: Advances in Modern Statistical Theory and Applications: A Festschrift in Honor of Morris L. Eaton, Institute of Mathematical Statistics, 2013, pp. 102–125.
[51] Q. Wu, et al., Survey of locomotion control of legged robots inspired by biological concept, Sci. China F 52 (10) (2009) 1715–1729.
[52] S. Garrido-Jurado, R. Muñoz-Salinas, F.J. Madrid-Cuevas, M.J. Marín-Jiménez, Automatic generation and detection of highly reliable fiducial markers under occlusion, Pattern Recognit. 47 (6) (2014) 2280–2292.
[53] K. Weinmeister, P. Eckert, H. Witte, A.-J. Ijspeert, Cheetah-cub-S: Steering of a quadruped robot using trunk motion, in: 2015 IEEE International Symposium on Safety, Security, and Rescue Robotics (SSRR), IEEE, 2015, pp. 1–6.
[54] Q. Shi, J. Gao, S. Wang, X. Quan, G. Jia, Q. Huang, T. Fukuda, Development of a small-sized quadruped robotic rat capable of multimodal motions, IEEE Trans. Robot. (2022).
[55] P. Lucas, S. Oota, J. Conradt, A. Knoll, Development of the neurorobotic mouse, in: 2019 IEEE International Conference on Cyborg and Bionic Systems (CBS), IEEE, 2019, pp. 299–304.

[56] C. Song, H. Feng, Y. Chen, I. Chen, R. Kang, Reconfigurable mechanism generated from the network of Bennett linkages, Mech. Mach. Theory 88 (2015) 49–62.

[57] X. Ma, K. Zhang, J.S. Dai, Novel spherical-planar and Bennett-spherical 6R metamorphic linkages with reconfigurable motion branches, Mech. Mach. Theory 128 (2018) 628–647.

[58] X. Chai, X. Kang, D. Gan, H. Yu, J.S. Dai, Six novel 6R metamorphic mechanisms induced from three-series-connected Bennett linkages that vary among classical linkages, Mech. Mach. Theory 156 (2021) 104133.

[59] Z. Song, Z. Luo, G. Wei, J. Shang, A portable six-wheeled mobile robot with reconfigurable body and self-adaptable obstacle-climbing mechanisms, J. Mech. Robot. (2022) 1–39.

[60] Z. Luo, J. Shang, G. Wei, L. Ren, A reconfigurable hybrid wheel-track mobile robot based on Watt II six-bar linkage, Mech. Mach. Theory 128 (2018) 16–32.

[61] H. Huang, B. Li, Geometric design of a bio-inspired flapping wing mechanism based on bennett-derived 6R deployable mechanisms, in: International Design Engineering Technical Conferences and Computers and Information in Engineering Conference, Vol. 46377, 2014, V05BT08A042.

[62] T. Li, C. Zhang, S. Wang, J.S. Dai, Jumping with expandable trunk of a metamorphic quadruped robot—The origaker II, Appl. Sci. 9 (9) (2019) 1778.

[63] C. Zhang, J. Dai, Trot gait with twisting trunk of a metamorphic quadruped robot, J. Bionic Eng. 15 (6) (2018) 971–981.

[64] C. Zhang, J.S. Dai, Continuous static gait with twisting trunk of a metamorphic quadruped robot, Mech. Sci. 9 (1) (2018) 1–14.

[65] K. Zhang, J.S. Dai, A kirigami-inspired 8R linkage and its evolved overconstrained 6R linkages with the rotational symmetry of order two, J. Mech. Robot. 6 (2) (2014) 021007.

[66] A. Sanchez-Gonzalez, N. Heess, J.T. Springenberg, J. Merel, M. Riedmiller, R. Hadsell, P. Battaglia, Graph networks as learnable physics engines for inference and control, in: International Conference on Machine Learning, PMLR, 2018, pp. 4470–4479.

[67] J. Tan, T. Zhang, E. Coumans, A. Iscen, Y. Bai, D. Hafner, S. Bohez, V. Vanhoucke, Sim-to-real: Learning agile locomotion for quadruped robots, 2018, arXiv preprint arXiv:1804.10332.